

A High-speed Large-range Tip-tilt-piston Micromirror Array

Jonathan B. Hopkins¹, Robert M. Panas¹, Yuanping Song, and Carolyn D. White

Abstract—This work introduces the design of a high fill-factor (>99%) micromirror array (MMA) that consists of 1mm^2 hexagonal mirrors, which are expected to each independently achieve continuous, closed-loop control of three degrees of freedom (DOFs)—tip, tilt, and piston—over large ranges ($>\pm 10^\circ$ rotation and $>\pm 30\mu\text{m}$ translation) at high speeds ($\sim 45\text{kHz}$ for a 1° amplitude of rotational oscillation). The flexure topology of this array is designed using the Freedom, Actuation, and Constraint Topologies (FACT) synthesis approach, which utilizes geometric shapes to help designers rapidly consider every flexure topology that best achieves a desired set of DOFs driven by decoupled actuators. The geometry of this array’s comb-drive actuators are optimized in conjunction with the geometry of the system’s flexures using a novel approach. The analytical models underlying this approach are verified using finite element analysis (FEA) and validated using experimental data. The capabilities of this new mirror array will enable, or significantly improve, the performance of a variety of high-impact optical technologies such as advanced optical switches, spatial-light modulators, displays, and laser steering or scanning devices.

Index Terms—Micromirror Array, Comb Drive Optimization, Flexure Bearings, Beam Steering, FACT Approach, MEMS

I. INTRODUCTION

Micromirror arrays (MMA) have demonstrated potential for advancing a wide range of applications including optics [1], [2], telecommunication [3], astronomy [4], [5], and display technologies [6], [7]. If such arrays could themselves be advanced such that they could cover larger areas while simultaneously achieving higher fill factors, larger ranges of motion, and higher speeds, existing technologies could be significantly enhanced and new technologies would emerge

Manuscript received September 12, 2016. This work was performed under the auspices of the U.S. Department of Energy by Lawrence Livermore National Laboratory under contract DE-AC52-07NA27344. LLNL-JRNL-702806-DRAFT. The authors gratefully acknowledge the help of Julie A. Jackson, Timothy M. Uphaus, William L. Smith, Christopher Harvey, and Steve Hunter from Lawrence Livermore National Laboratory for helping to collect the experimental data.

J. B. Hopkins and Y. Song are with the Department of Mechanical and Aerospace Engineering, University of California, Los Angeles, CA 90095 USA (e-mail: hopkins@seas.ucla.edu; adamsong@ucla.edu).

R. M. Panas is with the Materials Engineering Division, Lawrence Livermore National Laboratory, Livermore, CA 94550 USA (e-mail: panas3@llnl.gov).

C. D. White is with AM Fitzgerald & Associates, LLC, 700 Airport Blvd, Burlingame, CA 94010 USA (e-mail: cdw@amfitzgerald.com).

¹J. B. Hopkins and R. M. Panas are co-first authors on this paper as their contributions are equal.

within these and other applications. Moreover, the ability to independently and accurately control the position of each mirror within such MMAs in a continuous and repeatable fashion over their full range of motion in three degrees of freedom (DOFs)—tip, tilt, and piston—would also greatly advance and create new high-impact technologies. Such technologies may include (i) autostereoscopic displays that direct different projected images into the individual eyes of each viewer [8], (ii) high-speed focusable Light Detection And Ranging (LiDAR) technologies that could image rapidly moving objects or provide on-the-fly detailed feature interrogation, and (iii) additive fabrication systems that utilize spatial light modulators to both rapidly generate and scan 3D holograms for assembling large numbers of particles using principles of optical tweezers [9] or for curing large regions of photopolymers.

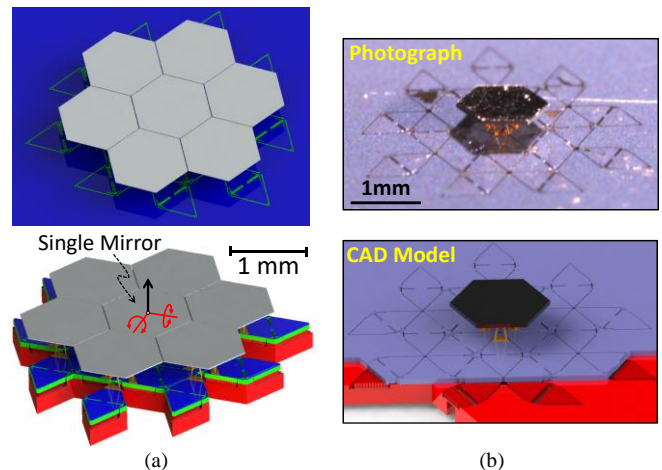


Fig. 1. New tip-tilt-piston MMA design (a); a single fabricated mirror (b)

In this paper, we introduce a new MMA design, shown with only seven mirrors in Fig. 1a, that is predicted to achieve the performance capabilities necessary to enable such technologies. These capabilities include a >99% fill factor, independent continuous closed-loop control of each $\sim 1\text{mm}^2$ hexagonal mirror over $>\pm 10^\circ$ in both tip and tilt (i.e., $>40^\circ$ optical steering range) and $>\pm 30\mu\text{m}$ in piston, and speeds up to $\sim 45\text{kHz}$ for a 1° amplitude of oscillation in tip and tilt. The new MMA design also possesses a transmission feature that can be tuned for specific applications such that the array’s mirrors can achieve a much larger range of motion than these metrics but with a slower speed, or achieve a much higher speed with a smaller range of motion. A single mirror of this new MMA was built as

a prototype to demonstrate fabrication feasibility (Fig. 1b), but the array’s design is suited to accommodate many mirrors that together cover large surface areas.

Specific contributions of this paper include the introduction of (i) a new MMA design that achieves advanced capabilities due largely to its sophisticated flexure topology, and (ii) a new optimization approach that utilizes simplified analytical models to rapidly determine the best comb-drive actuator geometry for achieving the fastest mirror speed given a general flexure topology.

Since the 1980s when Texas Instruments developed one of the first commercialized MMA devices (i.e., the Digital Mirror Device or DMD [7]), the rapid development of MEMS technology gave rise to hundreds of other MMA designs. A comprehensive review paper on the performance of all of these designs is a future work of the authors. This review paper will comparatively highlight the performance capabilities of this paper’s MMA design in the context of existing designs. Noteworthy designs that share similar features or achieve similar capabilities to the design of this paper are, however, referenced here. Stanford Microphotonics Lab developed a MMA design that utilizes a transmission to achieve tip-tilt-piston motions via electrostatic combs [10]. V. Milanovic *et al.* [11] from Adriatic Research Institute developed several tip-tilt-piston MMA designs that also use electrostatic combs. J. B. Stewart *et al.* [12] developed a tip-tip-piston MMA with hexagonal mirrors, which was commercialized by Boston Micromachines. A similar actuator design was later used in a continuous membrane surface design developed by Boston Micromachines [13]. The Biophotonics & Microsystems Laboratory at the University of Florida developed several MMA designs actuated by electrothermal bimorphs [14], [15]. Other MMA designs of note include J. Tsai *et al.* [16], M. Kim *et al.* [17] and H. Yu *et al.* [18], [19].

II. MICROMIRROR ARRAY DESIGN

The MMA design introduced in this paper is shown in Fig. 1a. Each mirror in this array is constrained from below by flexures that only permit three DOFs—two orthogonal rotations (shown as red lines with circular arrows about their axes in Fig. 1a) and an orthogonal translation (shown as a black arrow in Fig. 1a). A single hexagonal mirror within the repeating array is shown with different views in Figs. 2a-b. An exploded view of the system is shown in Fig. 2c.

The mirror is constrained by three identical axisymmetric serial flexure limbs called decoupled actuation limbs arranged in parallel. Each of these limbs consists of two parallel flexure subsystems stacked in series. One parallel subsystem consists of two wire flexures labeled “Decoupling Flexures” in Fig. 2c (colored yellow) that form a triangular truss and join the mirror to one of its three paddles labeled (1) through (3) in the same figure (colored blue and green). The other parallel subsystem consists of six flexure blades called actuator bearings that join the corresponding paddle to the fixed wafer called the “Actuation Plate” in Fig. 2c (colored red). Four of these flexures, labeled “ $r2$ Flexure Blades” in Fig. 2d, lie on the top surface of their corresponding paddle (colored blue) whereas

the other two flexures, labeled “ $r1$ Flexure Blades” in the same figure, lie on a plane that intersects and is perpendicular to the plane of the $r2$ flexure blades and is located in the middle of the paddle. Thus, the topology of this second parallel flexure subsystem (i.e., the actuator bearing) only permits its paddle to rotate about a single axis located at the intersection of these two planes. The rotational axis of paddle (1), for example, is labeled R_{paddle} in Fig. 2a.

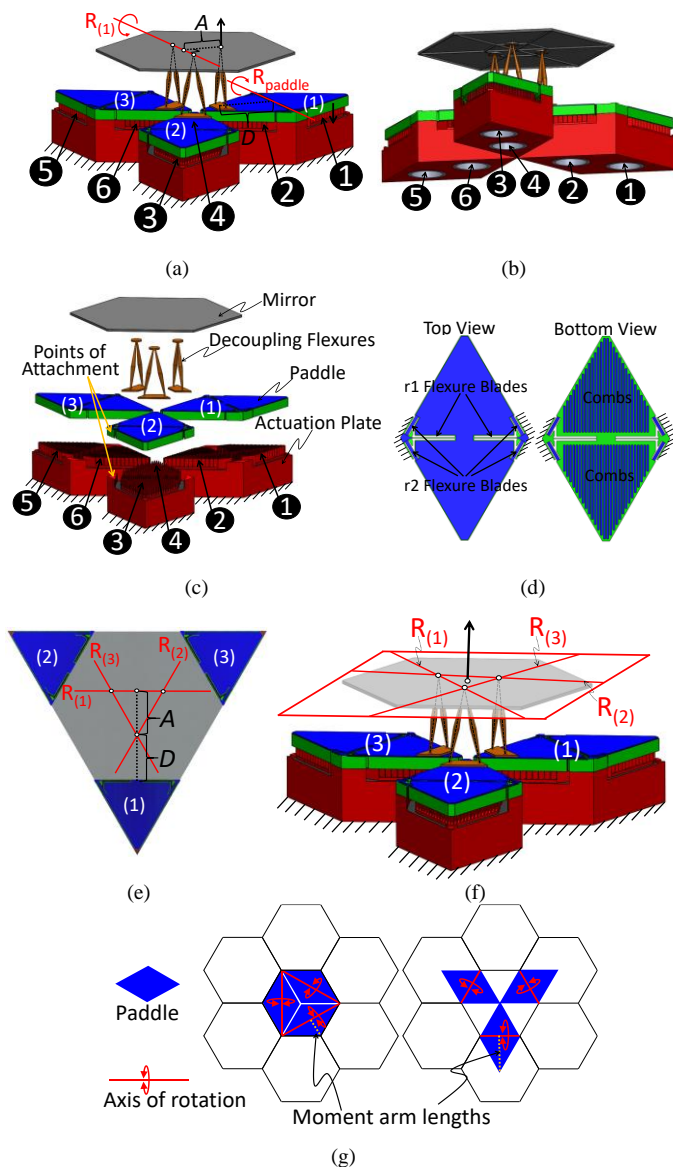


Fig. 2. Single mirror within the array—above view (a), below view (b), exploded view (c), paddle geometry showing the actuator bearing topology (d), bird’s-eye view (e), mirror freedom space (f), and two different ways to utilize the full area under the hexagon mirror using three axisymmetric paddles that are also symmetric about their axis of rotational (g). Note that larger views of the mirror design are provided in Supplemental Materials Section SI to clarify its finer features further.

The permissible rotation of each paddle is driven by a bipolar electro-static comb-drive actuator that consists of two separate sets of comb teeth that mesh with the teeth of the two regions underneath their corresponding paddle, labeled “Combs” in Fig. 2d. Each set of meshing combs on the actuation plate,

labeled 1 through 6 in Fig. 2c (colored red), can be independently charged with a voltage by a corresponding via that passes through the plate's backside where controller electronics are attached. These vias are also labeled 1 through 6 in Fig. 2b (colored grey) according to the number assigned to their corresponding set of comb teeth. Note that the paddles are all electrically grounded such that an electrostatic stress can be induced on the side of a particular paddle with combs that mesh with the set of combs that are electrically charged with a voltage from their corresponding via. If the via labeled 1 is given a charge, for instance, its corresponding paddle will pull down and rotate about R_{paddle} in the direction shown in Fig. 2a. If the other two paddles are simultaneously held fixed, the mirror will rotate about the axis labeled $R_{(1)}$ in Fig. 2a in the direction shown. To rotate the mirror about the same axis, but in the opposite direction, the via labeled 2 should be given a charge instead of the via labeled 1. Similarly, the mirror can be rotated about the axes labeled $R_{(2)}$ and $R_{(3)}$ (Figs. 2e-f) in different directions by charging vias 3 or 4 that correspond with paddle (2) and vias 5 or 6 that correspond with paddle (3) respectively. Thus, the mirror's six actuation vias can be independently charged by control electronics to drive any combination of $R_{(1)}$, $R_{(2)}$, and $R_{(3)}$. By charging these six actuation vias different amounts, the mirror can be made to translate along the axis of the black arrow shown in Fig. 2f or rotate about any axis that lies on the plane shown outlined red in the same figure—including the desired tip and tilt axes shown in Fig. 1a. Since this plane is defined by the three intersection points of each pair of wire flexure axes, shown as dashed black lines in the geometry of the decoupling flexures of Fig. 2f, the plane can be tuned to lie on any plane that is parallel to the mirror's face. Two good location options to choose for this plane are at the mirror's top surface or at the mirror's center of mass depending on where the tip and tilt axes are desired.

In addition to this *ability to tune the location of the mirror's desired tip and tilt axes by adjusting the intersection points of the wire flexures within the design's decoupling flexures*, the design possesses other advantageous features that contribute to its advanced performance. Note that *the fewest number of actuators have been employed to fully actuate the desired system DOFs* (i.e., three paddles are used to drive the mirror's desired three DOFs where each paddle requires two vias to drive each DOF in both directions). Thus, no redundant actuators exist to waste precious space.

The mirror's flexure topology is also largely symmetric and exactly-constrained [20] to achieve maximum precision with minimal thermal drift and parasitic error over its full range of motion. Each of the design's three identical decoupled actuation limbs uniquely constrain one of the mirror's three unwanted DOFs leaving only the three desired tip, tilt, and piston DOFs (i.e., none of the limbs contribute redundant constraint). Furthermore, each pair of wire flexures (i.e., the decoupling flexures) within each decoupled actuation limb are also exactly-constrained and thus don't contribute redundant constraint either. The only source of over-constraint in the design comes from the redundant flexure blades within the actuator bearings (Fig. 2d) that join the paddles to the actuation

plate. These actuator bearings are, however, purposely over-constrained to (i) achieve sufficient paddle stiffness to enable the mirror's optimal speed, (ii) render the design possible to fabricate (other purely exactly-constrained designs would be much harder to fabricate), and (iii) enforce symmetry about the paddles' axes of rotation. Paddle symmetry is important to help prevent the paddles from drifting as ambient temperatures fluctuate, to reduce parasitic error over the paddles full range of rotation, and to balance the paddle's inertia so that dynamically induced vibrations are minimized. Most of the negative effects caused by the choice to over-constrain the actuator bearings are mitigated by the fact that the redundant flexure blades are made from the same wafer and thus do not require traditional assembly. Furthermore, these flexure blades will likely avoid appreciable temperature gradients, which are harmful to over-constrained designs, because of their close proximity and high thermal-conductivity-to-thermal-expansion ratio (they are made of silicon). Note that if the entire array shown in Fig. 1 is subject to a change in temperature, the mirror can only displace along the direction of its translation/piston DOF because of symmetry. This minor potential for thermal drift will not affect the light steering capability of the overall system but could slightly influence its ability to modulate the light's phase if some mirrors in the array are subject to different changes in temperature than others.

The flexure topology of this paper's MMA design is also not under-constrained [20]. A system is under-constrained when any of its stacked parallel flexure subsystems possess redundant DOFs. Thus, when the stage of an under-constrained system is held fixed, one or more of its intermediate bodies possess one or more permissible motions that are not fully constrained and are thus susceptible to unwanted and uncontrolled vibrations. Note that for this paper's design, if its mirror is held fixed, the three paddles will be fully constrained (i.e., the paddles can't move). Note also that if all the paddles are held fixed, the mirror is totally exactly-constrained by an effective hexapod. If two paddles are held fixed, the mirror is only free to rotate with the unique motion caused by the paddle that was not held fixed. Thus, the controller used to dynamically drive this mirror can be simplified and does not need to compensate for poor mechanical design since every DOF in the system is accounted for and can be directly controlled by the system's actuators.

The MMA design's flexure topology also decouples its actuators. Note from Fig. 2a that regardless of how much paddle (1) is rotated by charging either vias 1 or 2, the other two paddles remain largely unaffected and experience no harmful forces as the mirror is rotated about the $R_{(1)}$ axis. Thus, the desired mirror DOFs can be independently actuated without requiring the actuation plate's combs (i.e., the system's actuators) to move during operation, which is the case for stacked actuator designs. Thus, this design achieves high speed in part because its actuators are designed to be stationary and because each paddle can be driven to independently actuate the mirror without causing the other paddles to move appreciably. As a result, the amount of mass that is necessary to accelerate to

achieve any desired mirror DOF is optimally minimized. This decoupling effect also greatly reduces the system’s control complexity and eliminates harmful stresses imposed on the system’s actuator bearings.

The design’s mirror is shaped like a hexagon for a number of reasons. A circular mirror would be the optimal geometry for a tip-tilt mirror from the standpoint of balanced mass moments of inertia. As long as a circular mirror rotates about an axis that lies on its plane and intersects its central point, the mass moment of inertia associated with that rotation is the same regardless of which axis is actuated (i.e., tip, tilt, or any combination of the two). Unfortunately, however, circles cannot fill space and would thus achieve an array with a reduced fill factor. Only three repeating regular polygon options exist that can fully fill space—equilateral triangles, squares, and regular hexagons. Of these three options, *hexagons are the most circle-like in that they possess the most balanced moments of inertia.*

Hexagons also enable a significant actuation advantage based solely on their geometry. Regardless of the regular polygon chosen for the mirror within any space-filling array, the maximum area that can be allotted to the bipolar electro-static rotary comb drive actuators is the area of the mirror’s polygon itself. Thus, an optimal design should utilize this full area to enable the maximum number of combs that can be packed for achieving the largest possible loads to drive the mirror with the highest possible speeds. It is difficult to divide the area under a square into three axisymmetric paddles for driving the mirror’s three DOFs. Such a design would require a fourth and thus, redundant actuation paddle to be axisymmetric, which would dramatically increase the system’s control complexity. Although both a triangle and a hexagon can be divided into three such axisymmetric paddles, *only the hexagon can be divided into three axisymmetric paddles that utilize the full area of the mirror’s polygon and are themselves symmetric about their axis of rotation (Fig. 2g).* This paddle symmetry, like a balanced seesaw, simplifies the dynamic control of the system. *Furthermore, note that a hexagon-mirror’s paddles can be made to fully utilize the allotted area of the hexagon in a way that also allows them to trade area real-estate under neighboring mirrors as shown on the right side of Fig. 2g. Using this configuration, the paddles can impart a significantly larger moment load to their corresponding mirror (i.e., >1.5x) because their moment arm lengths are substantially increased.* Thus, to optimize the speed with which the mirrors of the design of this paper can be driven, the configuration shown on the right side of Fig. 2g is used.

Finally, note that the flexure topology of the design of this paper possesses a double transmission effect that can be tuned to achieve a large variety of desired mirror speeds and ranges of motion. If each set of decoupling flexures (Fig. 2c), are moved the same amount toward the center of the mirror such that the parameter labeled D in Fig. 2a and Fig. 2e increases and the parameter labeled A decreases within each of the system’s three decoupled actuation limbs, the mirror’s rotational range increases substantially while its driving torque and speed capability decreases. In like manner, moving these decoupling

flexures away from the mirror’s center toward its edge substantially increases the mirror’s driving torque and speed capability while decreasing its rotational range. Thus, by simply arranging the position of the decoupling flexures within the mirror design of this paper, the mirror can be tuned to achieve a much larger range of motion or speed than those specified in Section I depending on the application intended for the MMA. Note also that the length along which the decoupling flexures can be displaced is substantially larger for the configuration on the right side of Fig. 2g compared with the configuration on the left side. This optimally large transmission-displacement length is another reason a hexagon mirror is chosen instead of a triangle or square mirror.

The flexure topology of the MMA design of this paper was synthesized using an advanced version of the Freedom, Actuation, and Constraint Topologies (FACT) synthesis approach that is geared toward enabling the synthesis of general multi-axis flexure systems with decoupled actuators [20]. FACT utilizes a complete library of intuitive geometric shapes that represent the mathematics of screw theory to help designers rapidly visualize and compare the flexure topologies that best achieve the desired performance capabilities while also satisfying other design and fabrication constraints. The specific FACT geometric shapes used to synthesize this paper’s MMA design as well as a discussion of why these shapes were selected are provided in Supplemental Materials Section SI.

The MMA design of this paper will achieve closed-loop continuous control of each mirror within the array by using the design’s electrostatic comb drives to not only actuate the system’s paddles, but also to sense their position and thereby back out the position of their respective mirrors using advanced dynamic models and system characterization. Others have successfully used electrostatic comb-drives to both actuate and sense similar systems [21] for similar control scenarios.

III. MODAL ANALYSIS

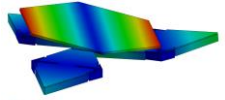
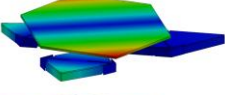
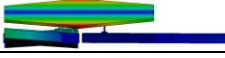
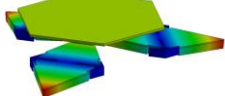
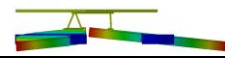
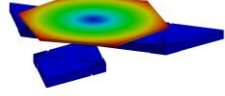
This section provides a modal analysis of two different versions, called ‘Fabricated’ and ‘Final’, of the MMA design discussed in Section II to assess how well the design’s FACT-synthesized topology achieves its three target DOFs—tip, tilt, and piston. The MMA topology’s geometric parameters are symbolically labeled in Fig. 3a-d.

For the first version of the design, called ‘Fabricated’, these parameters are defined to be the dimensions of the initial prototype of the MMA shown in Fig. 1b. The geometric parameters of this first-version prototype were conservatively defined with the primary objective of successfully demonstrating fabrication feasibility—not performance. The specific parameters for this ‘Fabricated’ version are provided in Table I. Note that one of the parameters, labeled in Fig. 3d, is a misalignment error, δ , between the paddle’s comb teeth and the actuation plate’s comb teeth. It is important to take this geometric parameter into consideration since the paddle layer is aligned and bonded to the actuation plate wafer during fabrication.

For the second version of the design, called ‘Final’, these parameters are defined to be the dimensions that will be used

that changing the decoupling flexures from HDDA to carbon or titanium would increase this difference and improve the system’s flexure performance further.

TABLE II
FINITE ELEMENT MODAL ANALYSIS OF THE TWO DESIGN VERSIONS

Mode Shape	Fabricated	Final
	1 st Mode: Tip	1 st Mode: Tip
	Natural Frequency: 1.9kHz	Natural Frequency: 4.5kHz
	2 nd Mode: Tilt	2 nd Mode: Tilt
	Natural Frequency: 1.9kHz	Natural Frequency: 4.5kHz
	3 rd Mode: Piston	3 rd Mode: Piston
	Natural Frequency: 2.8kHz	Natural Frequency: 4.7kHz
	4 th Mode: Torsion	4 th Mode: Torsion
	Natural Frequency: 9.9kHz	Natural Frequency: 35.4kHz
	5 th Mode: Shear	This mode is associated with a natural frequency greater than 60kHz
	Natural Frequency: 15.7kHz	

IV. COMB DRIVE OPTIMIZATION

In this section, we introduce a new analytical method for modeling and optimizing the geometry of comb drive actuators that can be tuned to achieve the largest actuation loads for driving flexure systems of a specified geometry with the highest possible speeds. This new optimization method limits unwanted pull-in displacement of the comb teeth to a controlled fraction of the gap between the teeth while considering fabrication misalignment errors and the stiffness of the full comb-drive’s load-path loop.

The task of successfully optimizing comb-drive systems has been an area of extensive research prior to this work. Particular comb-drive issues of interest have included the study of instabilities caused by pull-in forces on comb teeth [26]–[30], the stiffness of flexure bearings on comb-drive systems [27], and the effect of combs with varying cross-sectional areas [28]. While most past research efforts have typically focused on optimizing a system’s flexure bearing geometry for a given comb geometry [26], [27], [29], [30], this paper’s contribution is significant in part because it focuses on optimizing a system’s comb geometry for a given flexure bearing geometry and tipping range (i.e., the reverse scenario).

To optimize the geometry of this paper’s comb-drive

actuators, the mirror’s desired tipping range about its central axis parallel to the x-axis shown in Fig. 3a (e.g., $\pm 10^\circ$) is specified as a functional requirement. Note that to achieve this tipping motion for quasi-static loading conditions, the sets of actuation-plate combs labeled 4 and 6 in Fig. 3A must each impart half the force on their respective paddles as the force imparted by the set of actuation-plate combs labeled 1 on its paddle (Fig. 3a). Once the desired tipping range is provided for this actuation scenario, the system’s flexure geometry is then tuned such that the system’s rigid bodies are permitted to move over their full ranges of motion without causing the system’s flexures to yield or buckle. With a viable flexure geometry identified, the geometry of the comb drive actuators are then optimized using the theory of this section. Since the comb geometry can be fully defined using three independent parameters: (i) the width of paddle’s comb teeth w_p , (ii) the width of the actuation-plate’s comb teeth w_a , and (iii) the nominal gap between opposing comb teeth, d , as shown in Fig. 3d, the goal of this section’s optimizer is to determine the best values for these three parameters such that the mirror can be driven with the fastest speed possible.

It is important to recognize that the designs that achieve the fastest speeds are those with actuators that impart the largest driving loads on their respective paddles. Those designs will be the designs that (i) contain the most comb teeth possible with geometries that are equal to or larger than the smallest feature size that can be fabricated, and (ii) come closest to shorting due to electrical breakdown or comb-teeth pull-in when the largest possible voltage is supplied for the worst case misalignment error, δ . Although Paschen’s law dictates that electrical breakdown typically occurs between silicon comb teeth at 300V [31], the maximum voltage, V_{max} , allowed for the design of this paper is conservatively set to be 200V. Thus, the best design will impart the largest actuation load on its paddles by using a maximum threshold of 200V without failing due to pull-in of the comb teeth.

It is thus important to recognize where in the comb-drive actuators the pull-in failure will first occur to determine a conservative failure criterion. That location will be where the ratio between the pull-in force acting on the meshed comb teeth to the stiffness between those teeth is highest (i.e. the location where the maximum comb displacement occurs). FEA simulations demonstrate (Fig. 4a) that when the paddle is rotated its full range, this location occurs on the paddle’s longest comb tooth at $\sim 3/4$ of the way down the length of L_o , labeled in Fig. 3c. It is at this maximum paddle rotation that the largest pull-in force, F_p , labeled in Fig. 3d, will occur between the misaligned comb teeth since the maximum paddle rotation will produce the largest trapezoid-shaped overlapping area, A_{max} , between the longest comb tooth on the paddle, shown in Fig. 4a, and the nearest neighboring comb tooth on the actuation plate. The equation for this pull-in force, $F_p(x_p)$, as a function of the net pull-in displacement of the longest comb teeth, x_p , (i.e., the sum of the displacements of the top surfaces of both comb teeth as they deform toward each other with respect to the fixed actuation plate as shown in the upper right portion of Fig. 3d) and other previously defined parameters

(e.g., A_{max} , V_{max} , and δ and d as labeled in Fig. 3d), is provided in Supplemental Materials Section SII. The stiffness, k_{tot} , of the total load path loop from the longest comb tooth on the paddle through the paddle's flexure blades (i.e., actuator bearings) and on through to the closest neighboring comb tooth on the actuation plate can be calculated to relate the maximum pull-in displacement, x_p , to the pull-in force, $F_p(x_p)$, at the location of failure according to

$$\sum F_x = F_p(x_p) - k_{tot}x_p = 0. \quad (1)$$

Note that k_{tot} is also provided in Supplemental Materials Section SII and is a function of (i) the bending stiffness of the longest comb tooth on the paddle (i.e., k_p in Fig. 3d), (ii) the bending stiffness of the neighboring comb tooth on the actuation plate (i.e., k_a in Fig. 3d), and (iii) the stiffnesses of the $r1$ and $r2$ flexure blades (Fig. 2d) that correspond with the paddle's translational displacement along the x-axis (i.e., k_{rx} in Fig. 3d) and the paddle's rotation displacement about the z-axis (i.e., $k_{r\theta z}$ in Fig. 3d) but adapted so that these stiffness values all pertain to where pull-in failure occurs (i.e., $3L_c/4$ down the length of the longest paddle comb tooth as shown in Fig. 4a).

Using (1), an expression for the maximum pull-in displacement, $x_p(w_p, w_a, d)$ can be determined as a function of the desired independent comb parameters, w_p , w_a , and d . This expression is provided in Supplemental Materials Section SII. Pull-in failure will occur when x_p exceeds a critical threshold, which must be set to a conservative fraction of the shortest distance, $d - \delta$, between the misaligned meshed comb teeth (Fig. 3d). In a simple electrostatic parallel-plate actuator, consisting of one electrically grounded flat plate placed next to another charged flat plate, the threshold for pull-in failure typically occurs when the relative plate displacement (i.e., x_p) is 1/3 of the nominal gap between the plates. The addition of another electrically grounded plate on the other side of the charged plate that is slightly farther from the charged plate than the original grounded plate due to a misalignment error, δ , would increase this threshold because it would induce a pulling force on the charged plate in the opposite direction. It has been demonstrated, however, that the influence of this additional plate becomes insignificant as this misalignment error increases causing the threshold to converge back down to 1/3 of the nominal gap between the initial plates [27]. Thus, it is conservative to set the pull-in failure threshold of the comb-drive actuators of this paper's design to be $(d - \delta)/3$.

Thus, by setting the analytical expression of $x_p(w_p, w_a, d)$ to this threshold value according to

$$x_p(w_p, w_a, d) = \frac{d - \delta}{3}, \quad (2)$$

and by not allowing any feature to be smaller than the smallest size that can be fabricated, the optimal combination of independent actuator parameters, w_p , w_a , and d , can be identified that produce a geometry that operates at the safe pull-in limit without failing and is capable of imparting the largest possible maximum actuation torque on the paddles,

τ_{pmax} , without exceeding the maximum voltage limit, V_{max} . An expression for τ_{pmax} is provided in Supplemental Materials Section SII. Note that this optimization will always produce a conservative design that will never fail due to shorting, but will predict actuation performance that is always less than what the real design's actuators could actually achieve. The reason for this is that the optimization process always imposes (i) a conservative maximum voltage limit, (ii) a worst-case wafer misalignment error, (iii) a conservative pull-in failure threshold, (iv) a maximum worst-case pull-in force when the paddles are rotated their maximum amount, and (v) a conservatively compliant load-path loop that neglects various sources of stiffness. These neglected sources of stiffness include (i) the stiffness of other load-path loops that pass from the actuation plate, through the other two paddles, to the mirror, down to the paddle of interest, and back to the actuation plate, (ii) the extra stiffness caused by the large deformation stiffening of the paddle's actuator bearings as the paddle is tilted over its full range, and (iii) the stiffness caused by the paddle's side walls. Note that during the optimization process, the bending stiffness of the paddle's comb teeth are modeled as if they are only attached to the roof of the paddles and not attached to the surrounding side walls.

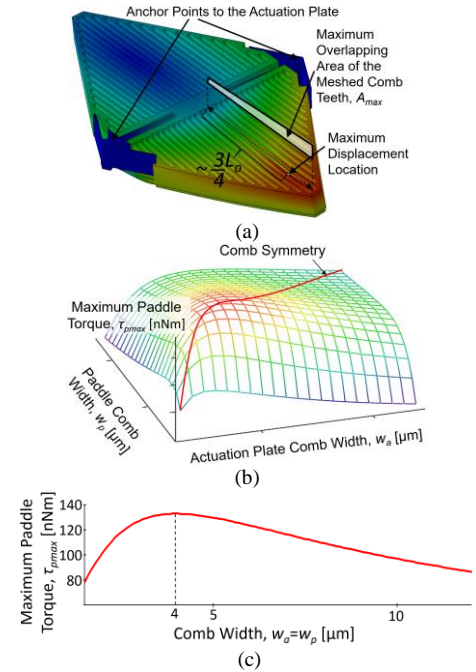


Fig. 4. FEA of the charged combs showing the location of the maximum pull-in displacement (a), plot of the maximum paddle torque output (b), and a cross-section along this plot's plane of symmetry for equal comb widths (c).

If the mirror's desired tipping range about its central axis parallel to the x-axis shown in Fig. 3a is set to $\pm 10^\circ$, and the 'Fabricated' version's flexure topology dimensions from Table I are applied along with the material properties provided in Section III, the optimization approach of this section generates the plot shown in Fig. 4b. This plot shows how designs with different actuator parameters, w_p and w_a , can impart different maximum torque values on their respective paddles, τ_{pmax} . Note that (2) reduces the number of unknown independent actuator

parameters from three to just two (i.e., w_p and w_a) since d can be calculated once the optimal values of w_p and w_a are identified. Note also from Fig. 4b that the design with the largest τ_{pmax} occurs along the symmetric cross section of the plot (shown as a red curve) when $w_p=w_a$. Thus, this symmetry effectively allows only one independent actuator parameter to be optimized (i.e., comb width). The symmetry of the plot in Fig. 4b results from simplified boundary condition assumptions within the stiffness expression of k_{tot} . A plot of the symmetric cross-section is provided in Fig. 4c. According to this plot, the best actuator design that can conservatively impart the largest τ_{pmax} on its paddles possess a paddle and actuation-plate comb width of $4\mu\text{m}$. Furthermore, note from Table I that these comb widths can be used to calculate the optimal gap distance, d , which is also $4\mu\text{m}$. Note that the actuator dimensions given in Table I for both the ‘Fabricated’ and ‘Final’ versions of the design were determined using the optimization approach of this section.

V. MIRROR SPEED ANALYSIS

In this section, closed-form analytical expressions are provided for calculating the maximum tipping speed of the MMA design’s mirror about the axis shown in Fig. 3a once the design’s comb-drive geometry has been optimized for a given set of flexure dimensions and a maximum mirror tipping range. The maximum tipping speed of a micromirror can be expressed as a stepping frequency, f_s , which is defined as the maximum frequency at which a mirror can be driven with a sinusoidal motion from resting at one angle to resting at another angle with an amplitude of rotation or step, θ_{step} . This stepping frequency, f_s , can be calculated according to

$$f_s = \frac{1}{\pi} \sqrt{\frac{2 \cdot \alpha_{max}}{\theta_{step}}}, \quad (3)$$

where α_{max} is the maximum mirror angular acceleration achieved during its sinusoidal motion. This angular acceleration can be calculated using the system’s first natural frequency, f_n , according to content provided in Supplemental Materials Section SIII. This natural frequency corresponds with the desired tipping mode shape shown as the first mode shape in Table II and in Fig. 3a. This natural frequency, f_n , can be calculated by

$$f_n = \frac{1}{2\pi} \sqrt{\frac{k_{\theta_{mtot}}}{J_{mtot}}}, \quad (4)$$

where $k_{\theta_{mtot}}$ is the mirror’s tipping stiffness that relates the effective torque imparted on the mirror by the system to the rotation of the mirror about the axis shown in Fig. 3a, and J_{mtot} is the system’s effective mass moment of inertia about the same axis. Equations for these values as well as derivations for (3) and (4) are provided in Supplemental Materials Section SIII.

Thus, by applying (3) to the ‘Fabricated’ version of the design specified in Table I, the resulting mirror’s stepping frequency with a fixed rotational amplitude of $\theta_{step}=1^\circ$ is expected to be 15.8kHz. For the ‘Final’ version of the design

with the same fixed amplitude, the stepping frequency is expected to be $\sim 45\text{kHz}$ as specified in Section I.

VI. FEA VERIFICATION AND EXPERIMENTAL VALIDATION

In this section, FEA and experimental data are applied to verify and validate key portions of the analytical theory used to optimize and predict the performance of the proposed MMA design.

FEA was applied to verify the analytical theory used to calculate the predicted pull-in displacement of the paddle’s comb teeth as given in (1) and in supplemental materials. This FEA was performed on the computer-aided-design (CAD) model of the paddle and its flexure-blade actuator bearings as shown in Fig. 4a, which was created using the ‘Fabricated’ dimensions given in Table I and was assigned the material properties of silicon provided in Section III. The model was held fixed at the locations where it would anchor to the actuation plate, and a pull-in force load was evenly distributed over all the maximum trapezoid-shaped overlap areas (Fig. 4a) on one side of each of the paddle’s comb teeth as if the paddle was rotated its full range. The FEA results verify that the maximum pull-in displacement occurs at $\sim 3L_o/4$ down the length of the longest paddle comb tooth. Furthermore, the FEA results show a maximum pull-in displacement of $0.61\mu\text{m}$, whereas the analytical tools of this paper predict a displacement of $0.67\mu\text{m}$ (i.e., 9.8% error).

FEA was also applied to verify the analytical theory used to calculate the micromirror’s predicted maximum tipping speed (i.e., stepping frequency) as provided in (3), (4), and in Supplemental Materials Section SIII. A single-mirror system was modeled and analyzed using FEA as shown in Table II. Using the ‘Fabricated’ version dimensions and the material properties specified in Section III, the FEA results show that the first natural frequency, which corresponds with the desired tipping mode shape, is 1.9kHz, whereas the analytical tools of this paper (i.e., (4)) predicts a natural frequency of 1.8kHz (i.e., 5.3% error).

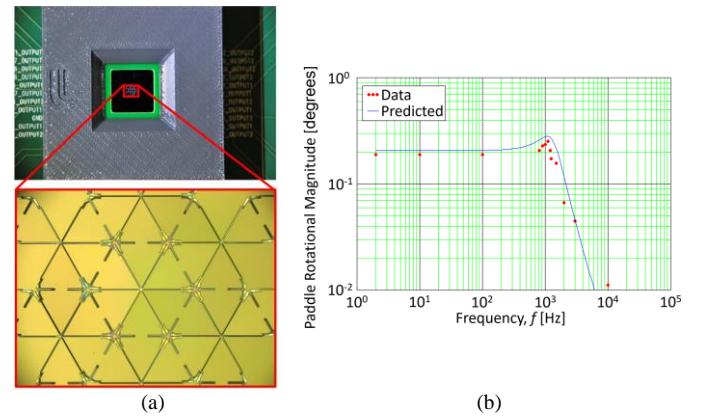


Fig. 5. Fabricated chip of an array of paddles on an actuation plate with driving circuitry (a), and a Bode plot of the paddles with r/l flexure blades only (b).

Preliminary data was also collected and applied to validate key portions of the analytical tools of this paper. Although a single mirror prototype of the ‘Fabricated’ version was

successfully made with all of its intended features as shown by the photograph of Fig. 1b, a simplified array of paddles was fabricated with the same dimensions but without the $r2$ -flexure-blade actuator bearings (i.e., only the $r1$ flexure blades were used) to test the system's electronics. These paddles were bonded to their complementary actuation-plate wafer, which was wired to control circuitry on a chip (Fig. 5a). This chip was used to characterize the dynamic performance of the paddles by generating the data that constitutes the Bode plot of Fig. 5b. As the figure demonstrates, the data validates the predicted paddle performance, which was determined using this paper's analytical tools as described in Supplemental Materials Section SIV.

VII. CONCLUSIONS AND FUTURE WORK

This paper introduces the design of a new array of hexagonal micromirrors that are expected to achieve a >99% fill factor, independent continuous closed-loop control of each millimeter-sized mirror over $\pm 10^\circ$ in both tip and tilt (i.e., $>40^\circ$ optical steering range) and $\pm 30\mu\text{m}$ in piston, and speeds up to $\sim 45\text{kHz}$ for a 1° amplitude of oscillation in tip and tilt. The design is also equipped with a transmission feature, which can be tuned to increase or decrease these performance capabilities to enable a variety of new high-impact applications. Analytical models were used to predict these capabilities and to optimize the system's actuator geometry. These models were verified and experimentally validated using FEA and preliminary data. A fabrication-demonstration prototype was also built.

Future work will include the following. The authors will soon publish a micromirror review paper, which plots the performance capabilities of published micromirror array designs from academia and industry. The authors will also create a more advanced optimization approach with more sophisticated non-linear analytical tools for identifying the optimal actuator and flexure geometries that will achieve the highest performance capabilities under high-speed large-deformation scenarios. The authors will also create a sophisticated control approach that will be informed by these new analytical tools to simultaneously and accurately control large numbers of mirrors. The authors will then fabricate a large array of the optimal mirror design and will use the control approach developed to experimentally validate its predicted performance in the context of practical applications.

REFERENCES

- [1] D. Débarre, E. J. Botcherby, T. Watanabe, S. Srinivas, M. J. Booth, and T. Wilson, "Image-based adaptive optics for two-photon microscopy," *Opt. Lett.*, vol. 34, no. 16, p. 2495, Aug. 2009.
- [2] N. Doble and D. R. Williams, "The Application of MEMS Technology for Adaptive Optics in Vision Science," *IEEE J. Sel. Top. Quantum Electron.*, vol. 10, no. 3, pp. 629–635, May 2004.
- [3] M. Yano, F. Yamagishi, and T. Tsuda, "Optical MEMS for photonic switching-compact and stable optical crossconnect switches for simple, fast, and flexible wavelength applications in recent photonic networks," *IEEE J. Sel. Top. Quantum Electron.*, vol. 11, no. 2, pp. 383–394, Mar. 2005.
- [4] P. A. Krulevitch, P. A. Bierden, T. Bifano, E. Carr, C. E. Dimas, H. Dyson, M. A. Helmbrecht, P. Kurczynski, R. S. Muller, S. S. Olivier, Y.-A. Peter, B. Sadoulet, O. Solgaard, and E.-H. Yang, "MOEMS spatial light modulator development at the Center for Adaptive Optics," in *Proceedings of SPIE*, 2003, vol. 4983, pp. 172–179.
- [5] I. W. Jung, Y.-A. Peter, E. Carr, J.-S. Wang, and O. Solgaard, "Single-Crystal-Silicon Continuous Membrane Deformable Mirror Array for Adaptive Optics in Space-Based Telescopes," *IEEE J. Sel. Top. Quantum Electron.*, vol. 13, no. 2, pp. 162–167, 2007.
- [6] Chun-da Liao and Jui-che Tsai, "The Evolution of MEMS Displays," *IEEE Trans. Ind. Electron.*, vol. 56, no. 4, pp. 1057–1065, Apr. 2009.
- [7] B. Lee, "DMD 101 : Introduction to Digital Micromirror Device (DMD)," 2013.
- [8] J. B. Hopkins and R. M. Panas, "Array Directed Light-field Display for Autostereoscopic Viewing," U.S. Patent 9 007 444, April 14, 2015.
- [9] L. A. Shaw, S. Chizari, R. M. Panas, M. Shusteff, C. M. Spadaccini, and J. B. Hopkins, "Holographic optical assembly and photopolymerized joining of planar microspheres," *Opt. Lett.*, vol. 41, no. 15, p. 3571, Aug. 2016.
- [10] I. W. W. Jung, U. Krishnamoorthy, and O. Solgaard, "High Fill-Factor Two-Axis Gimbaled Tip-Tilt-Piston Micromirror Array Actuated by Self-Aligned Vertical Electrostatic Combdrives," *J. Microelectromechanical Syst.*, vol. 15, no. 3, pp. 563–571, Jun. 2006.
- [11] V. Milanovic, G. A. Matus, and D. T. McCormick, "Gimbal-Less Monolithic Silicon Actuators for Tip-Tilt-Piston Micromirror Applications," *IEEE J. Sel. Top. Quantum Electron.*, vol. 10, no. 3, pp. 462–471, May 2004.
- [12] J. B. Stewart, T. G. Bifano, S. Cornelissen, P. Bierden, B. M. Levine, and T. Cook, "Design and development of a 331-segment tip-tilt-piston mirror array for space-based adaptive optics," *Sensors Actuators A Phys.*, vol. 138, no. 1, pp. 230–238, Jul. 2007.
- [13] S. a. Cornelissen, P. a. Bierden, T. G. Bifano, and C. V. Lam, "4096-element continuous face-sheet MEMS deformable mirror for high-contrast imaging," *J. Micro/Nanolithography, MEMS, MOEMS*, vol. 8, no. 3, p. 31308, Jul. 2009.
- [14] L. Wu, S. Dooley, E. a. Watson, P. F. McManamon, and H. Xie, "A Tip-Tilt-Piston Micromirror Array for Optical Phased Array Applications," *J. Microelectromechanical Syst.*, vol. 19, no. 6, pp. 1450–1461, Dec. 2010.
- [15] K. Jia, S. R. Samuelson, and H. Xie, "High-Fill-Factor Micromirror Array With Hidden Bimorph Actuators and Tip-Tilt-Piston Capability," *J. Microelectromechanical Syst.*, vol. 20, no. 3, pp. 573–582, Jun. 2011.
- [16] J. C. Tsai and M. C. Wu, "Gimbal-less MEMS two-axis optical scanner array with high fill-factor," *J. Microelectromechanical Syst.*, vol. 14, no. 6, pp. 1323–1328, 2005.
- [17] M. Kim, J.-H. Park, J.-A. Jeon, B.-W. Yoo, I. H. Park, and Y.-K. Kim, "High fill-factor micromirror array using a self-aligned vertical comb drive actuator with two rotational axes," *J. Micromechanics Microengineering*, vol. 19, no. 3, p. 35014, Mar. 2009.
- [18] H. Yu, H. Chen, J. J. Li, and J. J. Li, "Development of a novel 3×3 micromirror array for light modulation," *J. Micromechanics Microengineering*, vol. 14, no. 11, pp. 1544–1547, Nov. 2004.
- [19] H. Yu and H. Chen, "Development of a novel micromirror based on surface micromachining technology," *Sensors Actuators A Phys.*, vol. 125, no. 2, pp. 458–462, Jan. 2006.
- [20] J. B. Hopkins and D. McCalib, "Synthesizing multi-axis flexure systems with decoupled actuators," *Precis. Eng.*, vol. 46, pp. 206–220, Oct. 2016.
- [21] J. Dong and P. M. Ferreira, "Simultaneous actuation and displacement sensing for electrostatic drives," *J. Micromechanics Microengineering*, vol. 18, no. 3, p. 35011, Mar. 2008.
- [22] X. Zhang, X. N. Jiang, and C. Sun, "Micro-stereolithography of polymeric and ceramic microstructures," *Sensors Actuators, A Phys.*, vol. 77, no. 2, pp. 149–156, 1999.
- [23] E. Manias, J. Chen, N. Fang, and X. Zhang, "Polymeric micromechanical components with tunable stiffness," *Appl. Phys. Lett.*, vol. 79, no. 11, pp. 1700–1702, 2001.
- [24] C. Duty, D. Jean, and W. J. Lackey, "Laser chemical vapour deposition: materials, modelling, and process control," *Int. Mater. Rev.*, vol. 46, no. 6, pp. 271–287, Jun. 2001.
- [25] O. Lehmann and M. Stuke, "Three-dimensional laser direct writing of electrically conducting and isolating microstructures," *Mater. Lett.*, vol. 21, no. 2, pp. 131–136, Oct. 1994.
- [26] R. Legtenberg, a W. Groeneveld, and M. Elwenspoek, "Comb-drive actuators for large displacements," *J. Micromechanics Microengineering*, vol. 6, pp. 320–329, 1999.
- [27] T. T. Trutna and S. Awtar, "An Enhanced Stability Model for Electrostatic Comb-Drive Actuator Design," in *Proceedings of the ASME 2010 International Design Engineering Technical Conferences &*

Computers and Information in Engineering Conference IDETC/CIE 2010, 2010, pp. 1–9.

- [28] J. B. C. Engelen, L. Abelman, and M. C. Elwenspoek, “Optimized comb-drive finger shape for shock-resistant actuation,” *J. Micromechanics Microengineering*, vol. 20, no. 10, p. 105003, Oct. 2010.
- [29] J. D. Grade, H. Jerman, and T. W. Kenny, “Design of large deflection electrostatic actuators,” *J. Microelectromechanical Syst.*, vol. 12, no. 3, pp. 335–343, 2003.
- [30] M. Olfatnia, L. Cui, P. Chopra, and S. Awtar, “Large range dual-axis micro-stage driven by electrostatic comb-drive actuators,” *J. Micromechanics Microengineering*, vol. 23, no. 10, p. 105008, Oct. 2013.
- [31] T. Ono, D. Y. Sim, and M. Esashi, “Micro-discharge and electric breakdown in a micro-gap,” *J. Micromechanics Microengineering*, vol. 10, no. 3, pp. 445–451, Sep. 2000.



Jonathan B. Hopkins received his B.S., M.S., and Ph.D. degrees in mechanical engineering from the Massachusetts Institute of Technology (MIT), Cambridge, MA, USA, in 2005, 2007, and 2010, respectively. He was a postdoc at Lawrence Livermore National Laboratory (LLNL), Livermore, CA, USA, from 2010 to 2013.

He is currently an Assistant Professor at the University of California, Los Angeles (UCLA), Los Angeles, CA, USA, and is the director of the Flexible Research Group. His research interest is the design and fabrication of flexible structures, mechanisms, and materials. Specific areas of interest include microarchitected materials, precision flexure systems, MEMS, soft-robotics, compliant medical devices, and optics-based additive fabrication technologies.

Prof. Hopkins is an associate editor for *Precision Engineering* and is a member of the American Society for Precision Engineering (ASPE), the American Society of Mechanical Engineers (ASME), and the Materials Research Society (MRS). He was recently honored by President Barack Obama at the White House with a Presidential Early Career Award for Scientists and Engineers (PECASE) and is the 2016 recipient of ASME’s Freudenstein/General Motors Young Investigator Award.



Robert M. Panas received his B.S. degree in physics and his B.S., M.S., and Ph.D. degrees in mechanical engineering from the Massachusetts Institute of Technology (MIT), Cambridge, MA, USA, in 2007, 2009, and 2013, respectively.

He is currently a Research Engineer at the Lawrence Livermore National Laboratory (LLNL), Livermore, CA, USA. His research interests include precision engineering, MOEMS, additive micromanufacturing, and compliant mechanism design.

Dr. Panas is a member of the American Society for Precision Engineering (ASPE), is the chair of the ASPE Micro-Nano Technical Leadership Committee, was the chair of the ASPE Student Competition Committee for 2014-15, and received the NDSEG Fellowship 2008-11.



Yuanping Song received his B.S. degree in mechanical engineering from Shanghai Jiao Tong University, Shanghai, China, in 2012, and his M.S. degree in mechanical engineering from the University of California, Los Angeles (UCLA), Los Angeles, CA, USA, in 2014.

He is currently pursuing his Ph.D. degree as a graduate student researcher in Prof. Hopkins’ laboratory at UCLA. His research interests include the design, analysis, optimization, and control of microflexure-based MEMS devices.



Carolyn D. White received her B.S. in mechanical engineering from Brown University, Providence, RI, USA, in 1998, and M.S. and Ph.D. in mechanical engineering from the University of California, Berkeley, Berkeley, CA, USA, in 2003 and 2006.

She is an Associate at AMFitzgerald in Burlingame, CA, USA. She has a background in mechanics of materials and specializes in the design, analysis, and fabrication of MEMS devices for a wide range of applications, which have included electrostatic actuators, microfluidics, and piezoelectric devices. She has additional experience in technology strategic analysis including of the evaluation of patent portfolios, feasibility studies, and cost/performance analysis.

With 18 years of experience in MEMS, Dr. White is an active member of the MEMS & Sensors Industry Group, previously serving on its Technical Advisory Committee.

Supplemental Materials:

A High-Speed Large-Range Tip-Tilt-Piston Micromirror Array

Jonathan B. Hopkins, Robert M. Panas, Yuanping Song, and Carolyn D. White

SI. FLEXURE TOPOLOGY DESIGN USING FACT

This section describes how the theory introduced in [20] for using the Freedom, Actuation, and Constraint Topologies (FACT) approach to synthesize general multi-axis flexure systems with decoupled actuators was applied to synthesize the flexure topology of the MMA design of this paper. FACT utilizes a complete library of intuitive geometric shapes that represent the mathematics of screw theory to help designers rapidly visualize and compare the flexure topologies that best achieve the desired performance capabilities while also satisfying other design and fabrication constraints. The details of the systematic steps used to generate the flexure topology of this paper's MMA design are provided in [20], but this section briefly reviews the basic principles of FACT and provides the specific geometric shapes used to synthesize the flexure topology of this paper's MMA design as well as a discussion of why these shapes were selected.

According to FACT [20], every parallel flexure system (i.e., a system that consists of two rigid bodies directly joined together by flexible elements) possesses a freedom space and a complementary constraint space. A parallel flexure system's freedom space is a geometric shape that represents all the ways one of the bodies within the parallel subsystem is permitted to move with high compliance as a result of the deformation of its flexible elements (e.g., wire or blade flexure elements) when the other body in the system is held fixed. The system's complementary constraint space represents the region of space within which every viable flexible element could be placed to permit the motions within its freedom space while constraining other unwanted motions with high stiffness. It is important during the synthesis process that enough independent flexible elements are selected from a parallel flexure systems constraint space such that the resulting system will be permitted to move with the motions of its desired freedom space only. If too many flexible elements are selected from the constraint space such that some elements are redundant (i.e., they constrain the same motions), the system is over-constrained (i.e., it is not exactly-constrained). The process of appropriately selecting flexible elements from a system's constraint space such that the resulting system is exactly- or over-constrained to achieve the system's desired degrees of freedom (DOFs) has been addressed in many previous publications references in [20].

Consider the parallel flexure subsystem shown in Fig. S1a that consists of a single rigid paddle joined directly to the rigid actuation plate by six flexure blades (i.e. actuator bearings). This subsystem's constraint space is an infinite number of planes that intersect along a common axis as shown by the blue planes in Fig. S1a. Note from Fig. 2d that the paddle's two $r1$ flexure blades both lie on this constraint space's vertical plane labeled in Fig. S1a and the paddle's remaining four $r2$ flexure blades lie within the space's labeled horizontal plane. The constraint space's complementary freedom space is a single rotation line (Fig. S1b) that is collinear with the intersection axis of the constraint space's planes. Thus, the reason the paddle can only rotate about this axis is because a sufficient number of flexible elements were selected from within the subsystem's constraint space. As mentioned in the paper, however, this subsystem is over-constrained for a variety of beneficial reasons.

Now, consider the parallel flexure subsystem shown in Fig. S1c that consists of a rigid mirror joined directly to a rigid paddle by two angled wire flexure elements arranged in parallel. This system's constraint space is a disk of blue constraint lines that lie on the plane shown. Note that the axes of both wire flexure elements are collinear with constraint lines within the subsystem's constraint space. Its complementary freedom space (Fig. S1d) consists of (i) a plane of rotation lines that is coplanar with the constraint space's disk, (ii) a translation arrow that is orthogonal to this plane, (iii) a sphere of rotation lines that intersect at the intersection point of the constraint space's disk, and (iv) screw lines that are not shown in the figure to avoid visual clutter. Thus, if the paddle, shown in Fig. S1d, were held fixed, the mirror would be able to move with all of the motions within this freedom space because enough wire flexures were selected from the complementary constraint space. Note that the parallel system in Figs. S1c-d is exactly-constrained.

To determine the effective freedom space of the single serial limb (i.e., decoupled actuation limb) shown in Fig. S1e that consists of the two parallel subsystem's shown in Fig. S1b and Fig. S1d stacked together in series, the motions within the freedom spaces of both parallel subsystems should be linearly combined. Thus, if the rigid actuation plate were held fixed, a rigid mirror constrained by one of these serial limbs would not only be able to move with all the permissible motions within both parallel subsystem freedom spaces, shown on the left side of Fig. S1e, but the mirror would also be able to move with every combination of these motions. The resulting effective freedom space, shown on the right side of Fig. S1e, consists of (i) an infinite number of intersecting red planes that contain rotation lines, (ii) a disk of translation arrows that are perpendicular to the axis of intersection of these planes, and (iii) screw lines that are not shown to avoid visual clutter. This freedom space's complementary constraint space is a single constraint line that is collinear with the axis of intersection of the red planes in the freedom space. Thus, a mirror constrained by a single wire flexure element, like the one shown in Fig. S1f, is kinematically equivalent to the serial limb of Fig. S1e (i.e., it does the same job of both constraining and permitting the same motions). Note also that the serial limb of Fig. S1e is not under-constrained because neither of its two stacked constituent parallel subsystems possess redundant motions within their freedom spaces (i.e., the freedom space shown in Fig. S1b does

not lie within the freedom space shown in Fig. S1d when they are stacked as shown on the left side of Fig. S1e). Thus, if the mirror is held fixed with respect to the actuation plate, the paddle will be fully constrained and unable to move as well.

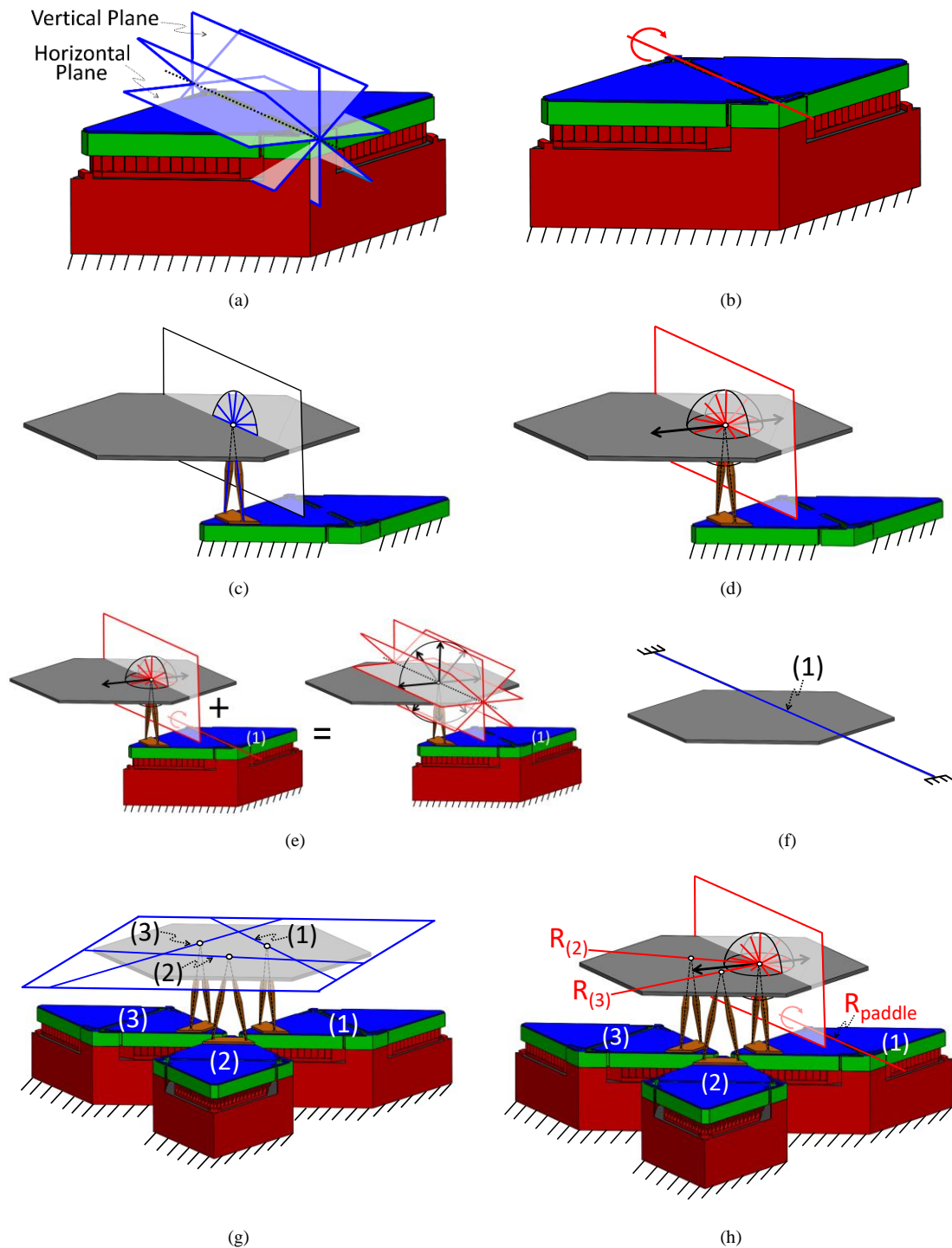


Fig. S1. Actuator bearings' constraint space (a) and freedom space (b); decoupling flexures' constraint space (c) and freedom space (d); decoupled actuation limb's effective freedom space (e) and effective constraint space (f); mirror's overall constraint space (g); and note that the freedom space of each limb's decoupling flexures satisfies the necessary conditions to correctly decouple the system's actuators (h).

To determine the overall effective constraint space of the entire single mirror system (Fig. S1g) that consists of three identical axisymmetric serial flexure limbs arranged in parallel, the effective constraint space of each serial limb must be linearly combined. Note that the effective constraint space of each serial limb (i.e., a single constraint line like the one shown in Fig. S1f) is shown and labeled according to its corresponding limb number in Fig. S1g. The constraint space that results from linearly combining these three constraint lines is the single plane shown outlined blue in the same figure. This space is the overall effective constraint space of the system's mirror. Its complementary freedom space is the red plane of rotation lines and the perpendicular translation arrow shown in Fig. 2f. Thus, if the actuation plate is held fixed, the overall flexure topology of the entire system is correctly designed to passively constrain each mirror within the array such that each mirror is only permitted to achieve the motions that result from the combination of the three desired DOFs (i.e., the tip, tilt, and piston motions shown in Fig. 1a). Note also that each mirror in the array is exactly-constrained by their three identical serial limbs because each limb, shown in Fig. S1e, only contributes a single effective constraint line on its corresponding mirror as shown in Fig. S1f.

According to FACT [20], the freedom space of the decoupling flexures (e.g., the wire flexures shown in Fig. S1d) within a decoupled actuation limb (e.g., the serial limb shown in Fig. S1e) must satisfy important conditions to optimally decouple their corresponding flexure system's actuators. The first condition is that the freedom space of the decoupling flexures must not contain the freedom space of the actuator bearings within the decoupled actuation limb such that their actuator can rigidly pass the intended displacement through the decoupling flexures to the system's stage (e.g., the mirror). For the design of this paper, the freedom space of the actuator bearing is the rotation line shown in Fig. S1b. Note from Fig. S1h that this line, labeled R_{paddle} , is not contained by the freedom space of the decoupling flexures (Fig. S1d and Fig. S1h) so the first condition is satisfied. If this line did belong within the freedom space of the decoupling flexures, the mirror would hardly move if the paddle were actuated. The second condition is that the freedom space of the decoupled actuation limb's decoupling flexures must contain all the stage motions that result from driving the actuators within the system's other decoupled actuation limbs. If this condition is satisfied, the stage motions induced by one actuator will minimally affect the other actuators within the system (i.e., the actuators will be decoupled). For this design, note from Fig. S1h that the motions $R_{(2)}$ and $R_{(3)}$, caused by actuating the paddles labeled (2) and (3) respectively, both lie in the sphere of rotation lines within the freedom space of the decoupling flexures that are driven by the paddle labeled (1). Thus, the MMA design of this paper satisfies the second condition as well so its actuators are optimally decoupled.

SII. COMB DRIVE OPTIMIZATION DETAILS

This section provides the details of the analytical tools used to model and optimize the geometry of the comb-drive actuators of this paper's MMA design. The goal of this optimization is to identify the best actuator geometry that drives the mirror with

the fastest speed for a given flexure-topology geometry. This new optimization method limits unwanted pull-in displacement of the comb teeth to a controlled fraction of the gap between the teeth while considering fabrication misalignment errors and the stiffness of the full comb-drive's load-path loop.

The pull-in force on the actuator's comb teeth, F_p , is produced by the electrostatic stress induced by the overlapping area between the comb teeth of the paddle and actuation plate. The largest pull-in force will occur when the paddle is rotated its maximum amount. This maximum force, imparted on the paddle's longest comb tooth, can be expressed as a function of the pull-in displacement, x_p , according to

$$F_p(x_p) = \frac{\varepsilon_r \varepsilon_0 A_{\max} V_{\max}^2}{2} \left(\frac{1}{(d - \delta - x_p)^2} - \frac{1}{(d + \delta + x_p)^2} \right), \quad (S1)$$

where ε_r is the relative permittivity of the air in the gap between the comb teeth, ε_0 is the permittivity of free space, A_{\max} is the maximum overlapping area of the paddle's longest comb tooth as labeled in Fig. 4a when the paddle is rotated its maximum amount, V_{\max} is the maximum allowable voltage limit (e.g., in this paper $V_{\max}=200V$ because of Paschen's law), d is the nominal gap distance between the meshed comb teeth as labeled in Fig. 3d, and δ is the worse-case misalignment error between comb teeth as labeled in Fig. 3d. The area, A_{\max} , has a trapezoidal shape and can be calculated according to

$$A_{\max} = L_o \cdot \left(d_o + \frac{\theta_{p\max}}{2} (2L_t - L_o) \right), \quad (S2)$$

where L_o is the length labeled in Fig. 3c and is essentially the length of the longest comb tooth in the paddle, d_o is the initial depth of meshed comb-tooth overlap (Fig. 3c) before the paddle is rotated, $\theta_{p\max}$ is the maximum angle the paddle can be rotated, L_t is the distance from the paddles' axis of rotation to the tip of the paddle as shown in Fig. 3c.

The pull-in force, F_p , is resisted by the full comb-drive loop-path stiffness, k_{tot} , (i.e. the stiffness from the paddle's longest comb tooth, through the actuator bearings, and onto the actuation plate's longest comb tooth nearest the paddle's longest comb tooth). To simplify the calculation of k_{tot} , the paddles and actuation plate are considered rigid bodies except for their comb teeth and the $r1$ and $r2$ flexure blades (i.e., actuator bearings) that join these two bodies. Although our stiffness analysis will conservatively ignore the stiffening effect on the paddle's comb teeth of their surrounding walls as the paper explains, it was observed that with these walls the location of maximum pull-in displacement always occurs near $\sim 3/4$ of the way down the length of L_o as shown in Fig. 4a. At this maximum pull-in displacement point, the overall stiffness, k_{tot} , is modeled as four different stiffness values arranged in series

according to

$$k_{tot} = \left(k_a^{-1} + k_p^{-1} + k_{rxn}^{-1} + k_{r\theta zn}^{-1} \right)^{-1}, \quad (S3)$$

where k_a is the bending stiffness of the longest comb tooth on the actuation plate shown in the top-right side of Fig. 3d, k_p is the bending stiffness of the longest comb tooth on the paddle shown in the top-right side of Fig. 3d, k_{rxn} is the modified translational stiffness of the $r1$ and $r2$ flexure blades along the x-axis shown in Fig. 3c for the case where the paddle is loaded at the point of maximum pull-in displacement, and $k_{r\theta zn}$ is the modified rotational stiffness of the $r1$ and $r2$ flexure blades about the z-axis shown in Fig. 3c for the case where the paddle is loaded at the point of maximum pull-in displacement. Note that all four of these stiffness values are defined as a force-to-displacement ratio at this location.

The bending stiffness of the actuation plate's longest comb tooth, k_a , is calculated by modeling the comb tooth as a cantilever beam according to

$$k_a = \frac{3 \cdot \frac{E_{Si}}{1 - \nu_{Si}^2} \cdot \frac{L_o w_a^3}{12}}{t_a^3}, \quad (S4)$$

where E_{Si} is the Young's modulus of silicon, modified for wide aspect ratio flexures, ν_{Si} is the Poisson's ratio of silicon, w_a is the width of the actuation plate's comb teeth labeled in Fig. 3d, and t_a is the height of the actuation plate's comb teeth along the z-direction as labeled in Fig. 3d.

The bending stiffness of the paddle's longest comb tooth, k_p , is calculated by assuming that the comb teeth are attached only to the paddle's roof—not their side walls. Therefore, k_p is also calculated as a cantilever beam according to

$$k_p = \frac{3 \cdot \frac{E_{Si}}{1 - \nu_{Si}^2} \cdot \frac{L_o w_p^3}{12}}{t_p^3}, \quad (S5)$$

where w_p is the width of the paddle's comb teeth labeled in Fig. 3d, and t_p is the height of the paddle's comb teeth along the z-direction as labeled in Fig. 3d.

The modified translational stiffness of the $r1$ and $r2$ flexure blades along the x-axis (Fig. 3c) for the case where the paddle is loaded at the point of maximum pull-in displacement, k_{rxn} , is calculated by scaling the actual translation stiffness of the $r1$ and $r2$ flexure blades along the x-axis, k_{rx} , shown in the top-left portion of Fig. 3d by a factor γ_{Nx} according to

$$k_{rxn} = \frac{k_{rx}}{\gamma_{Nx}}, \quad (S6)$$

where k_{rx} is

$$k_{rx} = 2 \left(\frac{E_{Si} \cdot t_{r1} \cdot w_{r1}}{L_{r1}} \right) + 4 \left(\sin^2(\theta_{r2}) \cdot \frac{12E_{Si} \cdot t_{r2} w_{r2}^3}{L_{r2}^3} + \cos^2(\theta_{r2}) \cdot \frac{E_{Si} \cdot t_{r2} w_{r2}}{L_{r2}} \right), \quad (S7)$$

and where t_{r1} , w_{r1} and L_{r1} are the dimensions of the $r1$ flexure blades labeled in Fig. 3c. Note also from Fig. 3c that θ_{r2} is the angle between the $r2$ flexure blades and the paddle's rotation axis, and t_{r2} , w_{r2} , and L_{r2} are the dimensions of the $r2$ flexure blades labeled in Fig. 3c. The factor γ_{Nx} in (S6) is the ratio between the maximum comb overlapping area on the paddle's longest comb tooth when the paddle is rotated its maximum amount, A_{max} , and the sum of all the comb overlapping areas within the entire paddle when it is rotated its maximum amount. This factor scales the pull-in force on the paddle's longest comb tooth to the total pull-in force on the entire paddle so that the total translation of the paddle along the x-axis is reflected in the pull-in displacement at the maximum pull-in displacement point at $\sim 3/4$ of the way down the length of L_o as shown in Fig. 4a. The factor, γ_{Nx} , is calculated according to

$$\gamma_{Nx} = \frac{1}{2} \cdot \frac{1 + \frac{\theta_{pmax}}{d_o} \left(L_t - \frac{2}{3} L_o \right)}{1 + \frac{\theta_{pmax}}{d_o} \cdot \left(L_t - \frac{1}{2} L_o \right)} \cdot \frac{\frac{L_o}{L_t} L_a}{w_a + w_p + 2d} \cdot \left(1 - \frac{2\sqrt{3}}{L_o^2} \left(L_a \cdot \frac{L_o}{L_t} w_{edge} + \left(w_{r2} + \frac{w_{edge}}{2} \right) \left(L_{r2} + L_{r20} - \frac{\sqrt{3}}{2} (L_t - L_o) \right) \right) \right), \quad (S8)$$

where L_a is the paddle dimension labeled in Fig. 3c, w_{edge} is the side-wall width at the edge of the paddle (Fig. 3c), and L_{r20} is the distance from the $r2$ flexure blade's anchor point to the paddle's axis of rotation as shown in Fig. 3c.

The modified rotational stiffness of the $r1$ and $r2$ flexure blades about the z-axis (Fig. 3c) for the case where the paddle is loaded at the point of maximum pull-in displacement, $k_{r\theta zn}$, is also calculated by scaling the actual rotational stiffness of the $r1$ and $r2$ flexure blades about the z-axis, $k_{r\theta z}$, shown in the top-left portion of Fig. 3d by another factor $\gamma_{N\theta z}$ according to

$$k_{r\theta zn} = \frac{k_{r\theta z}}{\gamma_{N\theta z}}. \quad (S9)$$

where $k_{r\theta z}$ is

$$k_{r\theta z} = 2 \left(\frac{E_{Si} \cdot \frac{t_{r1} w_{r1}^3}{12}}{L_{r1}} + \frac{12E_{Si} \cdot \frac{t_{r1} w_{r1}^3}{12}}{L_{r1}^3} \left(\frac{L_a - L_{r1}}{2} - L_{r10} \right)^2 \right) + 4 \left(\frac{E_{Si} t_{r2} w_{r2}}{L_{r2}} \left(\sin(\theta_{r2}) \cdot \frac{L_a}{2} - w_{r2} \right)^2 + \frac{12E_{Si} \frac{t_{r2} w_{r2}^3}{12}}{L_{r2}^3} \left(\cos(\theta_{r2}) \frac{L_a}{2} - L_{r2} - L_{r20} \right)^2 \right), \quad (S10)$$

and where L_{r10} is the distance from the $r1$ flexure blade's anchor point to the paddle's edge as shown in Fig. 3c. This rotational stiffness, $k_{r\theta z}$, is converted to the linear stiffness, $k_{r\theta zn}$, at the maximum pull-in displacement point using the scaling factor $\gamma_{N\theta z}$ according to (S9). This factor relates the pull-in force on the paddle's longest comb tooth to the total torque about the z-axis imparted on all the paddle's comb teeth. It also converts the rotation of the paddle about the z-axis to the displacement at the maximum pull-in displacement point. This factor, $\gamma_{N\theta z}$, is calculated according to

$$\gamma_{N\theta z} = \frac{1}{2} \frac{1 + \frac{\theta_{p\max}}{d_o} \left(\left(L_t - \frac{2}{3} L_o \right) + \frac{1}{18} \cdot \frac{L_o^2}{L_t - \frac{2}{3} L_o} \right)}{1 + \frac{\theta_{p\max}}{d_o} \cdot \left(L_t - \frac{1}{2} L_o \right)} \frac{L_a \frac{L_o}{L_t} \left(L_t - \frac{2}{3} L_o \right) \left(L_t - \frac{L_o}{4} \right)}{w_a + w_p + 2d} \cdot \left(1 - \frac{2\sqrt{3}}{L_o^2} \left(L_a \cdot \frac{L_o}{L_t} w_{edge} + \left(w_{r2} + \frac{w_{edge}}{2} \right) \left(L_{r2} + L_{r20} - \frac{\sqrt{3}}{2} (L_t - L_o) \right) \right) \right). \quad (S11)$$

Equation (1) from the paper was derived using principles of static equilibrium at the point of maximum pull-in displacement. A solution that captures the amount of pull-in displacement, x_p , at this point can be determined using (1) in conjunction with (S1) and (S3). However, to generate a simplified closed-form analytical expression of this solution, the solution can be approximated by simplifying (S1) via a second-order Taylor series approximation according to

$$F_p(x_p) \approx F_p(x_0) + \frac{dF_p(x_0)}{dx_p} (x_p - x_0) + \frac{1}{2} \frac{d^2F_p(x_0)}{dx_p^2} (x_p - x_0)^2, \quad (S12)$$

where x_0 is the Taylor series expansion value. This value must be chosen such that the solution to (1) will be in the vicinity of this value. Thus, a Taylor series expansion value of $x_0=(d-\delta)/6$ was selected for the optimization of this paper since the desired x_p

solution of (1) should be between 0 and $(d-\delta)/3$ (i.e., the pull-in failure threshold discussed in the paper). Thus, using (S12) with the chosen Taylor series expansion value and (S3), (1) can be solved to find

$$x_p(w_p, w_a, d) = \frac{1}{6}(d - \delta) - \frac{\frac{dF_p(x_0)}{dx_p} - k_{tot}^{-1} - C}{\frac{d^2F_p(x_0)}{dx_p^2}}, \quad (\text{S13})$$

where C is

$$C = \sqrt{\left(\frac{dF_p(x_0)}{dx_p}\right)^2 - 2F_p(x_0)\frac{d^2F_p(x_0)}{dx_p^2} + k_{tot}^{-1}\left(\frac{1}{3}(d - \delta)\frac{d^2F_p(x_0)}{dx_p^2} - 2\frac{dF_p(x_0)}{dx_p}\right) + k_{tot}^{-2}}. \quad (\text{S14})$$

The geometry of the comb-drive actuators can be fully defined by three independent parameters (i.e., w_p , w_a , and d). Thus, the goal of the optimization approach is to determine the optimal values of w_p , w_a , and d to identify the design that can impart the largest maximum torque, τ_{pmax} , on its paddles to drive its mirror with the highest speed for a given flexure topology geometry. This torque is calculated by integrating the electrostatic stress over the overlapping areas of the comb teeth according to

$$\begin{aligned} \tau_{pmax} &= 2 \left(1 - \frac{2\sqrt{3}}{L_o^2} \left(\frac{L_o}{L_t} L_a w_{edge} + \left(w_{r2} + \frac{w_{edge}}{2} \right) \left(L_{r2} + L_{r20} - \frac{\sqrt{3}}{2} (L_t - L_o) \right) \right) \right) \int_0^{\frac{1}{2}L_o} \int_{L_t - L_o}^{L_t - L_t \frac{2x}{L_o}} \frac{\epsilon_r \epsilon_0 V_{max}^2}{(w_a + 2d + w_p)d} y dy dx \\ &= \left(1 - \frac{2\sqrt{3}}{L_o^2} \left(\frac{L_o}{L_t} L_a w_{edge} + \left(w_{r2} + \frac{w_{edge}}{2} \right) \left(L_{r2} + L_{r20} - \frac{\sqrt{3}}{2} (L_t - L_o) \right) \right) \right) \frac{L_a \frac{L_o}{L_t} \left(L_t - \frac{2}{3} L_o \right)}{w_a + w_p + 2d} \frac{L_o \epsilon_r \epsilon_0 V_{max}^2}{2d}, \quad (\text{S15}) \end{aligned}$$

Thus, during the optimization process, the best values of w_p , w_a , and d are identified that (i) are equal to or larger than the smallest feature sizes that can currently be fabricated (i.e., w_p and w_a were set to not be smaller than $1.5\mu\text{m}$ and d was set to not be smaller than $2\mu\text{m}$ for the ‘Fabricated’ version of the design but to not be smaller than $1\mu\text{m}$ for the ‘Final’ version), (ii) satisfy the pull-in failure threshold criterion defined in (2) so that designs are identified that come closest to failing due to pull-in but do not fail, and (iii) produce designs that impart the largest values of (S15) without exceeding the maximum voltage limit, V_{max} . The optimization results are provided in the paper.

SIII. MIRROR SPEED ANALYSIS DETAILS

In this section, the derivation details of the closed-form analytical expression of

the maximum tipping speed (i.e. the stepping frequency given as (3) in the paper) of the MMA design's mirror about the axis shown in Fig. 3a are provided. According to (3), this stepping frequency is expressed as a function of the mirror's maximum angular acceleration, α_{max} , achieved under sinusoidal actuation. This angular acceleration is defined according to

$$\alpha_{max} = \theta_{mmax} \gamma_{\theta} (2\pi f_n)^2, \quad (S16)$$

where θ_{mmax} is the maximum mirror tipping range specified by the designer (e.g., $\pm 10^\circ$), and γ_{θ} is the ratio of the maximum torque that can be applied to the mirror, τ_{mmax} , as determined by the maximum voltage limit, V_{max} , and the torque imparted on the mirror that is required to tip the mirror over its full maximum tipping range, θ_{mmax} . This ratio is thus given by

$$\gamma_{\theta} = \frac{\tau_{mmax}}{k_{\theta tot} \theta_{mmax}}, \quad (S17)$$

where

$$\tau_{mmax} = \frac{3}{2} \cdot \gamma_{amp}^{-1} \tau_{pmax}, \quad (S18)$$

and where γ_{amp} is the system's amplification or transmission factor that is responsible for amplifying the rotations of the paddles to the mirror's rotations as discussed in the paper. This factor is defined according to

$$\gamma_{amp} = D/A_c, \quad (S19)$$

where D is the distance from the plane of the decoupling flexures to the paddle's axis of rotation as labeled in Fig. 2a, Fig. 2e, and Fig. 3a, and A_c is the distance from the plane of the decoupling flexures to the center of the mirror where the tipping axis passes as shown in Fig. 3a. Note that τ_{pmax} from (S18) is given by (S15). The angular stiffness, $k_{\theta tot}$, given in (S17) is defined as the ratio between the torque imparted on the mirror and the resulting angle over which the mirror is tipped about the axis shown in Fig. 3a. This angular stiffness is given by

$$k_{\theta tot} = \frac{3}{2} \gamma_{amp}^{-2} k_{r\theta} + 6(1 - \gamma_{amp}^{-1} + \gamma_{amp}^{-2}) k_{df\theta x} + \frac{3}{2} k_{df\theta y}, \quad (S20)$$

where $k_{r\theta}$ is the combined angular stiffness of the paddle's $r1$ and $r2$ flexure blades labeled in Fig. 2d about the paddle's axis of rotation labeled R_{paddle} in Fig. 2a. This stiffness is defined according to

$$k_{r\theta} = 2k_{r1\theta} + 4k_{r2\theta}. \quad (S21)$$

where $k_{r1\theta}$ is the angular stiffness of a single $r1$ flexure blade about the paddle's axis of rotation given by

$$k_{r1\theta} = \frac{\frac{E_{Si}}{2(1+\nu_{Si})} \cdot \frac{1}{1-\nu_{Si}^2} \cdot \frac{t_{r1} w_{r1}^3}{3} \left(1 - 0.63 \frac{w_{r1}}{t_{r1}} \left(1 - \frac{1}{12} \cdot \frac{w_{r1}^4}{t_{r1}^4} \right) \right)}{L_{r1}} + \frac{12E_{Si} \cdot \frac{1}{1-\nu_{Si}^2} \cdot \frac{t_{r1} w_{r1}^3}{12} \cdot \frac{t_{r1}^2}{4}}{L_{r1}^3}, \quad (S22)$$

and $k_{r2\theta}$ is the angular stiffness of a single $r2$ flexure blade about the paddle's same axis of rotation given by

$$k_{r2\theta} = \frac{\frac{E_{Si}}{2(1+\nu_{Si})} \cdot \frac{w_{r2} t_{r2}^3}{3} \left(1 - 0.63 \frac{t_{r2}}{w_{r2}} \left(1 - \frac{1}{12} \cdot \frac{t_{r2}^4}{w_{r2}^4} \right) \right)}{L_{r2}} \cos^2(\theta_{r2}) + \frac{4E_{Si} \cdot \frac{w_{r2} t_{r2}^3}{12} \left(1 + 3 \cdot \frac{L_{r20}}{L_{r2}} + 3 \cdot \left(\frac{L_{r20}}{L_{r2}} \right)^2 \right)}{L_{r2}} \sin^2(\theta_{r2}). \quad (S23)$$

The stiffness, $k_{df\theta x}$, in (20) is the angular stiffness of the decoupling flexures that join the mirror with the paddle labeled (1) in Fig. 3a about an axis that passes through the intersection of the axes of the decoupling flexures' two wire flexure elements and points in the direction of the x-axis labeled in the same figure. This stiffness is defined according to

$$k_{df\theta x} = 2 \cdot \frac{E_{Poly} \cdot \frac{\pi \cdot d_{df}^4}{64}}{L_{df}}, \quad (S24)$$

where E_{Poly} is the Young's modulus of hexanediol diacrylate (HDDA) polymer, d_{df} is the diameter of the wire flexure elements within the decoupling flexures labeled in Fig. 3b, and L_{df} is the length of these elements labeled in the same figure. The stiffness, $k_{df\theta y}$, in (20) is the angular stiffness of the decoupling flexures that join the mirror with the paddle labeled (1) in Fig. 3a about an axis that passes through the intersection of the axes of the decoupling flexures' two wire flexure elements and points in the direction of the y-axis labeled in the same figure. This stiffness is defined according to

$$k_{df\theta y} = 2 \cdot \frac{4E_{Poly} \cdot \frac{\pi \cdot d_{df}^4}{64}}{L_{df}} \cdot \left(1 + 3 \cdot \frac{L_{df0}}{L_{df}} + 3 \cdot \left(\frac{L_{df0}}{L_{df}} \right)^2 \right), \quad (S25)$$

where L_{df0} is the distance from the top of either of the two wire flexure elements within the decoupling flexures to the intersection point of their axes as shown in Fig. 3b.

The first natural frequency, f_n , of the mirror's tipping mode shape about the axis shown in Fig. 3a from (S16) is provided in (4) of the paper. This natural frequency is a function of $k_{\theta_{tot}}$ given in (S20), and is a function of the system's effective moment of inertia, J_{tot} , about the axis shown in Fig. 3a. This moment of inertia is defined according to

$$J_{tot} = J_m + \frac{3}{2} \gamma_{amp}^{-2} \cdot J_p, \quad (S26)$$

where J_m is the moment of inertia of the hexagon-shaped mirror about the axis shown in Fig. 3a given by

$$J_m = \frac{5\sqrt{3}}{16} \rho_{Si} t_m L_m^4, \quad (S27)$$

and where ρ_{Si} is the density of silicon, t_m is the mirror's thickness as labeled in Fig. 3b, and L_m is the side length of the mirror's hexagon as labeled in Fig. 3a and Fig. 3b. The term J_p in (S26) is the paddle's moment of inertia about the axis labeled R_{paddle} in Fig. 2a. This moment of inertia can be calculated according to

$$J_p = \frac{\sqrt{3}}{16} \rho_{Si} L_a^4 \left(\frac{w_p t_p}{w_a + w_p + 2d} + t_{roof} \right) + \rho_{Si} L_a^3 t_p w_{edge} + \left(\frac{\sqrt{3}}{2} \frac{\rho_{Si} w_p t_p L_a^2}{w_a + w_p + 2d} + 4 \rho_{Si} L_a t_p w_{edge} \right) \left(\frac{t_p}{2} \right)^2, \quad (S28)$$

where t_{roof} is the thickness of the paddle's roof labeled in Fig. 3d.

SIV. EXPERIMENTAL DATA VERSES PREDICTED PADDLE PERFORMANCE

This section explains the details of how the plot of Fig. 5b was generated. An array of paddles was fabricated (Fig. 5a) using the dimensions of the 'Fabricated' version of the design given in Table I, but without the four $r2$ flexure blades (i.e., the paddles were only constrained by the two symmetric $r1$ flexure blades) labeled in Fig. 2d. These paddles were driven by various sets of electrically charged comb teeth on the actuation plate underneath the paddles. The red dots of data in Fig. 5b were collected by measuring the movements of laser beams reflected off the top surfaces of the paddles to determine the magnitude of their rotational angles for various frequencies of oscillation.

The predicted dynamic performance of the fabricated paddles is depicted as a blue curve in the plot of Fig. 5b. This curve was analytically generated using a second-order dynamic model of the paddles. This model utilized the paddle's moment of inertia, J_p , provided in (S28), the combined angular stiffness of the paddle's actuator bearings about the paddle's axis of rotation, $k_{r\theta}$, provided in (S21) but using

$k_{r2\theta} = 0$ since the paddles possessed no r^2 flexure blades, and a damping ratio of 0.4, which was experimentally measured. Note from Fig. 5b that the resulting predicted performance closely matches the measured data.